Meccanica (2025) 60:2487–2506
https://doi.org/10.1007/s11012-025-01962-y

RESEARCH

A slip-transpiration-vortex model for riblets past the viscous regime

Alessandro Bottaro · Giulia Innocenti · Essam Nabil Ahmed

Received: 29 September 2024 / Accepted: 27 February 2025 / Published online: 24 March 2025

Abstract A new boundary condition at a plane, fictitious wall, meant to simulate the presence of small-scale streamwise-aligned riblets is outlined and tested. The need for an approach which extends beyond the *viscous regime* stems from the high cost of numerically resolving microscopic flow details within micro-ribs, and from the desire to rapidly optimize a variety of wall textures. A multiscale homogenization technique which accounts for advection is coupled to a synthetic vortex model which mimics the transverse flow in the near-wall region. The proposed wall model captures the non-monotonic behavior of the skin-friction drag over ribleted surfaces with the increase in ℓ^+ (the pitch distance measured in viscous units), including the performance degradation and the eventual drag increase beyond some ℓ^+ threshold.

Keywords Riblets · Asymptotic homogenization · Navier slip · Surface transpiration

A. Bottaro (✉) · G. Innocenti · E. N. Ahmed
DICCA, University of Genova, via Montallegro 1, 16145 Genova, Italy
e-mail: alessandro.bottaro@unige.it

G. Innocenti
e-mail: giulia.innocenti@edu.unige.it

E. N. Ahmed
e-mail: essameldin.abdo@edu.unige.it

1 Introduction

Riblets are streamwise-aligned microscopic grooves designed on surfaces to reduce skin friction. These tiny structures mimic the natural design of dermal denticles in the skin of sharks, whose unique texture inspired the development of riblets for use in fluid dynamics [1]. The history of riblet research dates back several decades, when Walsh and collaborators [2–4] documented early NASA experiments that indicated drag reductions on aircraft surfaces when riblets were applied, highlighting their potential for wide-scale use in commercial and military aviation. More recent studies [5] have shown that, once properly designed, riblets can reduce drag by up to 10%, making them a significant approach to pursue when fuel efficiency and speed are critical. In the aeronautical sector, riblets have been tested on aircraft fuselages, wings, and turbine blades. The ability to reduce drag can lead to substantial fuel savings over long flights, translating to lower operational costs and reduced environmental impact due to decreased carbon emissions. The reduction in fuel consumption is particularly crucial in the aviation industry, where even small improvements in aerodynamics can lead to massive cost savings.

In the maritime sector, riblets can be applied to the hulls of ships and submarines to reduce drag and enhance fuel efficiency. As in aeronautics, reduced drag in marine environments means that less energy is required to propel vessels through water, leading

to cost savings in fuel and higher speeds. The 1987 America's Cup yacht Stars & Stripes is perhaps the most famous example of the effectiveness of riblets in marine applications [6]; ongoing research in this field continues to explore their potential for commercial shipping and naval vessels, including the possible application that consists in impregnating riblets or riblet-like microstructures with a lubricant liquid [7].

Riblets can be fabricated using various techniques, including microfabrication, laser etching, and 3D printing [8], allowing engineers to create precise patterns that are tailored to specific applications. The scale of the riblets and the spacing between them must be carefully designed to match the size of the turbulent eddies that they are intended to control. Too large or too small riblets will fail to deliver the expected benefits, making the design process a critical aspect of their application. Probably, the most exhaustive set of experimental results for riblets is due to Bechert et al. [5]; different types of riblets (sawtooth, scalloped, blade and trapezoidal riblets, adjustable slits and ribs) of different spanwise wavelengths were tested in the Berlin zero-pressure gradient oil channel, measuring shear stress with both a high-accuracy balance and a Preston tube. The results were reported in terms of $DR = \Delta\tau_w/\tau_{w_0} \approx \Delta C_f/C_{f_0}$ (τ_w is the wall shear stress and C_f is the skin friction coefficient, $C_f = \dfrac{2\,\tau_w}{\rho \hat{u}_{bulk}^2}$, with $\hat{u}_{bulk}$ the outer/bulk speed and ρ the density of the fluid; subscript "0" denotes a smooth-wall value) versus the spanwise spacing of the riblets, $\ell^+ = \ell\, u_\tau/\nu$ (u_τ is the friction velocity and ν is the kinematic viscosity of the fluid), demonstrating the existence of a *viscous regime* for very closely spaced ribs with a linear reduction in skin friction, a subsequent peak in drag reduction, followed by an increase of the *DR* parameter which turns into a drag penalty for ℓ^+ exceeding a value of the order of 30. The viscous regime (for ℓ^+ less than $5 \div 10$, depending on the geometry of the riblets) is well described by the Stokes-based theory from Luchini et al. [9]. They proved that riblets offer a greater resistance to transverse flow than they do to the streamwise motion, and were able to characterize this different resistance quantitatively in terms of a longitudinal and a spanwise slip length, λ_x and λ_z respectively. Luchini el al. [9] argued also that, since the two slip lengths simply measure distances from the riblet tips (which represent but an arbitrary origin of the y axis), they hold no particular role in relation to the macroscopic flow. Any physically significant quantity cannot depend on the choice of the origin, whereas the same does not hold for the *difference* between the two slip lengths, $\Delta\lambda = \lambda_x - \lambda_z$. This was confirmed later by Luchini [10] and Jiménez [11], who were able to derive an expression for *DR*, i.e.

$$\begin{aligned} \frac{C_f - C_{f_0}}{C_{f_0}} &= -\frac{\Delta U^+}{(2\,C_{f_0})^{-1/2} + (2\,\kappa)^{-1}} \\ &= -\frac{\mu_0\,\Delta\lambda^+}{(2\,C_{f_0})^{-1/2} + (2\,\kappa)^{-1}}, \end{aligned} \tag{1}$$

with ΔU^+ the log-layer velocity difference (assumed positive when skin friction drag is reduced) and κ von Kármán's constant. The constant μ_0 depends on the riblets' shape and periodicity; it was reported to be approximately equal to 0.66 by Jiménez [11], 0.785 by Bechert et al. [5] and 1 by Luchini [10]. In particular, Luchini argued that the equality $\Delta U^+ = \Delta\lambda^+$ stems from the rigid upwards displacement of the origin of the mean turbulent flow profile, in the presence of riblets, for the increase in mean streamwise velocity to match the vertical displacement. This argument ceases to apply beyond the viscous regime, for ℓ^+ above a value of about ten.

The breakdown of the viscous regime, the presence of a peak in drag reduction for any given riblet shape and the subsequent deterioration in performance with the increase of ℓ^+, is less-well understood, although the first half of Eq. (1), which stems directly from Prandtl's skin friction law, is believed to maintain its validity for as long as the logarithmic region exists, i.e. as long as Townsend similarity hypothesis holds. An enticing analysis on the effect of advection on the drag-reduction breakdown has been put forward by Goldstein and Tuan [12]. Through direct numerical simulations of turbulence next to a solid surface with scalloped riblets, they showed that, as the spanwise periodicity of the micro-structures increases, the ability of the ribs' lateral walls to damp crossflow fluctuations is hampered, favouring the formation of secondary streamwise vortices through and above the ribs, increased vertical mixing and drag. Similar secondary pairs

of counter-rotating vortices were identified later also by Endrikat [13]. These observations motivate the present study, which aims to model advection above the grooves with a homogenization approach inspired by that of Luchini et al. [9], with the inclusion, however, of a zero-net-mass-flux transpiration boundary condition at a virtual surface positioned right above the riblets' tips.

The particular upscaling technique employed here goes by the name of *adjoint homogenization* [14] and allows inclusion of advection, a crucial ingredient when the periodicity of the wall texture is sufficiently large. Several studies have appeared in the literature in recent years, aimed at modeling the effect of micro-patterned walls on the overlying flow [15–20]. All previous studies, except for the very recent one by Ahmed and Bottaro [21], do not account for advection, not even in an approximate manner. The purpose of this work is to provide a fresh look at the theory, extending the concept of slip lengths (and interface permeability coefficients) by accounting for near-wall streamwise vortex structures. A similar attempt has been made recently by Wong et al. [22]; similarities and differences will be discussed in the following.

2 The upscaling approach

This section is dedicated to providing the details of the derivation of *effective* boundary conditions at the fictitious interface between a channel flow and a regularly microstructured wall. The multiple-scale, homogenization procedure builds upon the work by Bottaro & Naqvi [20], although it eventually differs in two respects:

1. Since turbulence is the object of the investigation, the expansion parameter does not use the channel thickness as macroscopic length scale but a length proportional to the viscous wall unit, ν/u_τ, on the assumption that the turbulent motion outside of the roughness sublayer is independent of roughness' shape and distribution. This hypothesis, which goes by the name of Townsend wall-similarity, loses validity when the roughness elements extend their effect into the outer layer, with consequent destruction of a significant portion of the log-law region [11].
2. In the model developed the convective terms of the Navier–Stokes equations remain at leading order when the equations are expanded in terms of a small parameter $\delta = \ell/\mathcal{L}$, with ℓ the microscale; this permits consideration of near-wall advection, which is expected to play a significant role when the riblets' periodicity, ℓ, exceeds a value of about 10 viscous units. This upscaled model of wall irregularities differs from all those described in recent papers [14–22].

Section 2.1 of the paper starts with a discussion of the scales adopted, followed by normalization of the equations in the two domains considered, the inner, or near-wall, domain, and the outer, or bulk, domain. After identifying a small perturbation parameter, δ, the expansion of the inner variables is performed and the inner-outer matching explained. The adjoint homogenization procedure [14] for the inner problem at leading order is outlined in Sect. 2.4, allowing to close the inner-outer matching at the boundary of the two domains. The important issue of the transpiration velocity at the fictitious boundary at $Y = 0$ is then addressed (Sect. 2.5); even if such velocity is formally of smaller order compared to the wall-parallel components, it plays an important role in turbulence near a rough wall, as demonstrated in a number of studies [23–25]. The most original contribution of the present paper is presented in Sect. 2.6, where it is assumed that the adjoint field develops on top of a streamwise-homogeneous mean flow plus a longitudinal vortex, function of the cross-stream coordinates, of periodicity equal to that of the riblets. Our synthetic vortex is meant to model the average vortex computed for the flow over riblets by Goldstein and Tuan [12], Endrikat [13], and Modesti et al. [26]. Slip and wall permeability coefficients are found for this new model and used in direct simulations of the turbulent flow over blade riblets. The results, reported in Sect. 3.2, show that the new model outperforms previous wall models in predicting the drag reduction curve, even for relatively large riblets' spacings.

2.1 Governing equations, domain decomposition and scaling arguments

Let us consider a wall corrugated by regularly arranged, streamwise-aligned solid protrusions, with given periodicity in the spanwise direction, $\hat{x}_3 = \hat{z}$.

The other dimensional spatial variables are $\hat{x}_1 = \hat{x}$ and $\hat{x}_2 = \hat{y}$. The longitudinal velocity component is denoted by $\hat{u}_1 = \hat{u}$, the wall-normal component is $\hat{u}_2 = \hat{v}$ and the spanwise velocity component is $\hat{u}_3 = \hat{w}$. We consider the turbulent flow in a channel of thickness $2H$ (cf. Fig. 1), driven by a constant streamwise pressure gradient $\partial\hat{p}/\partial\hat{x}_1$ which balances the resistance at the solid walls; the bulk speed in the channel is denoted by $\hat{u}_{bulk}$ and a friction velocity can be defined as $u_\tau = \sqrt{\tau_w/\rho}$, with τ_w the total stress at the wall and ρ the fluid density. In a turbulent channel flow the velocity profile is expected to behave linearly for small values of $\hat{y}$, with the streamwise component of the form:

$$\hat{u} = \hat{y}\,\frac{\tau_w}{\mu} + \text{constant}, \tag{2}$$

with μ the dynamic viscosity of the fluid. The constant in Eq. (2) is related to the position chosen for the $\hat{y} = 0$ plane whenever the solid surface is microtextured; for a smooth wall the constant vanishes on account of the no-slip condition.

It is now necessary to identify the physical length scales of the problem, in order to decide whether and when separation of scales is tenable. The need to estimate the order of magnitudes of the different terms is compelling in view, in particular, of the recent criticism to the use of multiscale theory on the ground that separation of scales holds only for very narrowly spaced riblets [22].

The microscopic characteristic length, $\tilde{\ell}$, of the problem can be estimated by the effect that the microstructured surface exerts on the overlying coherent structures; quasi-streamwise vortices penetrate below the rim of the riblets by a distance roughly equal to the transverse slip length. It is known that, for a variety of wall textures, such a length is much smaller than the periodicity of the patterns, ℓ; just for the purpose of setting ideas let us assume that $\tilde{\ell} \sim \frac{\ell}{\alpha}$, with α a number approximately equal to 15 (we will come back to this number later). The macroscopic scale, denoted by $\tilde{\mathcal{L}}$, is representative of the vortex size, i.e. typically 15 to 20 units of length in viscous units [27, 28]. To set ideas,

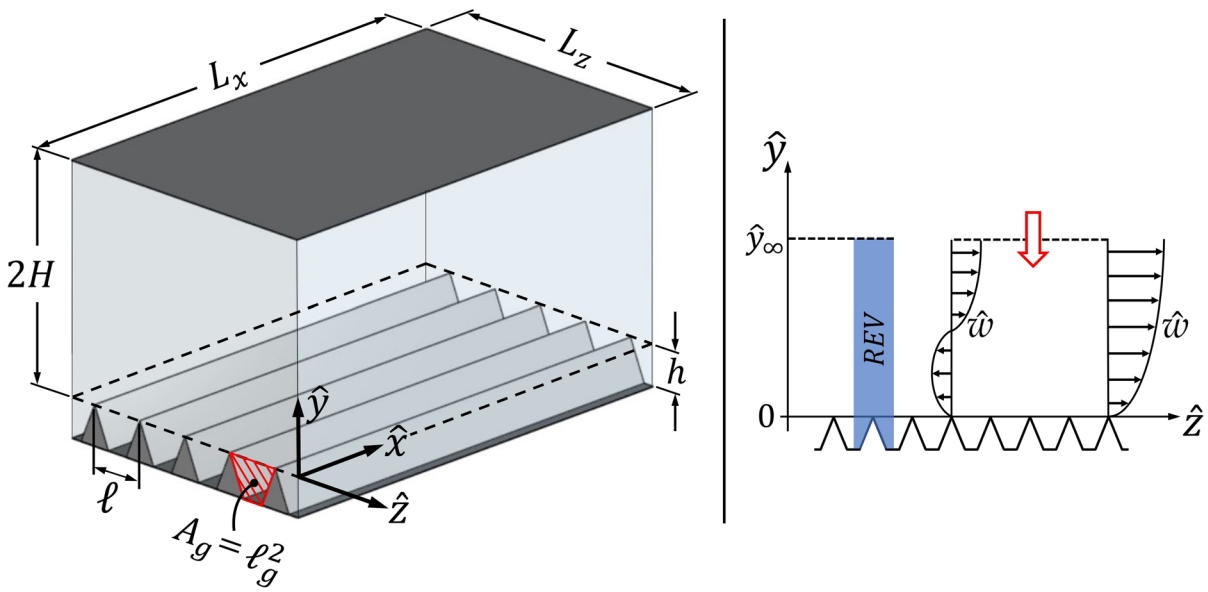

Fig. 1 Sketch of the problem under consideration, not to scale. In the left image, the surface delimited by the black dashed lines represents the *virtual boundary* where macroscopic, effective conditions are enforced. The dashed red surface defines the characteristic length scale ℓ_g of the riblets, whose spanwise periodicity is ℓ. The image on the right illustrates the representative elementary volume (*REV*), colored in blue, used to extract the coefficients of the effective boundary conditions, together with a sketch to explain the appearance of a wall-normal velocity component at $\hat{y}_\infty$ (red arrow) arising out of spanwise gradients of $\hat{w}$ (and/or streamwise gradients of $\hat{u}$)

the scale $\tilde{\mathcal{L}}$ is thus of order $\alpha\frac{\nu}{u_\tau}$, with α as before. The ratio between these two scales is thus

$$\frac{\tilde{\ell}}{\tilde{\mathcal{L}}} \sim \frac{\ell^+}{\alpha^2} = \alpha^{-2}\,\frac{\ell}{h}\,h^+, \tag{3}$$

with the plus superscript used to denote variables normalized in wall units and h the height of the riblets (cf. Fig. 1); the ratio ℓ/h is at the most equal to two in the present work so that its product with α^{-2} is ordinarily smaller than 10^{-2}. The quantity $h^+ = h\,u_\tau/\nu$ in Eq. (3) is the roughness Reynolds number whose value separates the flow regimes conventionally defined as hydrodynamically smooth ($h^+ \lesssim 5$), transitional ($5 \lesssim h^+ \lesssim 70$) and fully rough ($h^+ \gtrsim 70$). If we remain in the regime sometimes called *lower transitionally rough* [29], with h^+ roughly below 15, the ratio $\tilde{\ell}/\tilde{\mathcal{L}}$ is bounded from above by approximately 0.1, an acceptably low value for multiple scale theory to hold. Under the conditions just stated, the periodicity ℓ^+ of the riblets should be limited to about 30 viscous units. An *a posteriori* verification, based on direct numerical simulations using model interface conditions and comparisons with experiments and texture-resolving turbulent simulations, will be needed to confirm that separation of scales is tenable up to $\ell^+ \approx 30$.

Let us now estimate the magnitude of the velocity, near the patterned wall and at some distance from it, to assess comparatively viscous and advective terms in the microscopic Navier–Stokes equations. The outer velocity magnitude can be evaluated by Eq. (2) as being of order $\tilde{\mathcal{L}}\,\frac{\tau_w}{\mu} = \alpha u_\tau$. For shear stress to match at the outer boundary $\hat{y}_\infty$ of the representative elementary volume (cf. Fig. 1) the inner velocity scale must be equal to about $\frac{\tilde{\ell}}{\tilde{\mathcal{L}}}\,\alpha\,u_\tau$. The microscopic advective term $\hat{u}_j\frac{\partial \hat{u}_i}{\partial \hat{x}_j}$ is thus $\mathcal{O}(\alpha^2\frac{\tilde{\ell}\,u_\tau^2}{\tilde{\mathcal{L}}^2})$, while the viscous term $\nu\,\hat{\nabla}^2\hat{u}$ is $\mathcal{O}(\alpha\,\frac{\nu u_\tau}{\tilde{\mathcal{L}}\,\tilde{\ell}})$. Normalization of the Navier–Stokes equation yields a dimensionless number in front of the advective term which is given by

$$\alpha^{-2}\left[\frac{\ell\,u_\tau}{\nu}\right]^2 = \left[\frac{1}{\alpha}\left(\frac{\ell}{h}\right)h^+\right]^2. \tag{4}$$

The quantity above is sufficiently small only for values of h^+ equal to a few viscous units of length, meaning that the conventional approach based on the Stokes approximation of the equations to derive slip lengths [9] ceases to be valid away from the hydrodynamically smooth regime. When h^+ reaches the value of 15 the dimensionless parameter in Eq. (4) is of order one; this means that, despite the fact that separation of scales is tenable, the nonlinear term cannot be neglected any longer.

After this qualitative discussion on scales, needed for a preliminary evaluation of the limitations and validity of the proposed approach, we can proceed with the formal analysis, eliminating the empirical coefficient α from the scaling parameters, but keeping in mind the estimated magnitude of the different terms in the equations. Indicating with $\hat{t}$ the dimensional time variable, the mass and momentum conservation equations governing the flow of a viscous, incompressible, Newtonian fluid are:

$$\frac{\partial \hat{u}_i}{\partial \hat{x}_i} = 0, \quad \left(\frac{\partial \hat{u}_i}{\partial \hat{t}} + \hat{u}_j\frac{\partial \hat{u}_i}{\partial \hat{x}_j}\right) = -\frac{1}{\rho}\frac{\partial \hat{p}}{\partial \hat{x}_i} + \nu\frac{\partial^2 \hat{u}_i}{\partial \hat{x}_j^2}. \tag{5}$$

Now, we denote the outer region with superscript "$\mathcal{O}$", while for the near-wall, inner region the superscript "$\mathcal{I}$" is employed. The normalized variables in the two regions are the following:

Outer region $^{\mathcal{O}}$:

$$X_i = \frac{\hat{x}_i u_\tau}{\nu}, \quad P^{\mathcal{O}} = \frac{\hat{p}}{\rho u_\tau^2}, \quad U_i^{\mathcal{O}} = \frac{\hat{u}}{u_\tau}, \quad t^{\mathcal{O}} = \frac{\hat{t}u_\tau^2}{\nu}. \tag{6-a}$$

Inner region $^{\mathcal{I}}$:

$$x_i = \frac{\hat{x}_i}{\ell}, \quad P^{\mathcal{I}} = \frac{\hat{p}\,\ell}{\mu\,\hat{u}_{inner}}, \quad U_i^{\mathcal{I}} = \frac{\hat{u}}{\hat{u}_{inner}}, \quad t^{\mathcal{I}} = \frac{\hat{t}\,\hat{u}_{inner}}{\ell}, \tag{6-b}$$

with the microscopic velocity scale $\hat{u}_{inner} = u_\tau^2\ell/\nu$. The normalization above leads to the following dimensionless systems in the two regions:

$$\frac{\partial U_i^{\mathcal{O}}}{\partial X_i} = 0, \quad \frac{\partial U_i^{\mathcal{O}}}{\partial t} + U_j^{\mathcal{O}}\frac{\partial U_i^{\mathcal{O}}}{\partial X_j} = -\frac{\partial P^{\mathcal{O}}}{\partial X_i} + \frac{\partial^2 U_i^{\mathcal{O}}}{\partial X_j^2}, \tag{7-a}$$

$$\frac{\partial U_i^{\mathcal{I}}}{\partial x_i} = 0, \quad Re_{inner}\left(\frac{\partial U_i^{\mathcal{I}}}{\partial t} + U_j^{\mathcal{I}}\frac{\partial U_i^{\mathcal{I}}}{\partial x_j}\right) = -\frac{\partial P^{\mathcal{I}}}{\partial x_i} + \frac{\partial^2 U_i^{\mathcal{I}}}{\partial x_j^2}. \tag{7-b}$$

In the outer region of the flow all memory is lost of details of the microstructure, whereas variables in the inner region are assumed to depend on both ℓ and $\mathcal{L}$. The factor in front of the convective term in Eq. (7b) is the microscopic Reynolds number,

$$Re_{inner} = \frac{\hat{u}_{inner}\,\ell}{\nu}; \tag{8-a}$$

it coincides with the square of the gauge factor $\delta = \ell/\mathcal{L}$ which can also take the form

$$\delta = \epsilon Re_\tau = \ell^+, \tag{8-b}$$

with $\epsilon = \ell/H$, $Re_\tau = u_\tau H/\nu$ the friction Reynolds number in the plane channel and ℓ^+ the riblets' spacing measured in viscous units. Inner velocity and pressure fields are now expanded in powers of δ as

$$\Phi^{\mathcal{I}} = \phi^{(0)} + \delta\,\phi^{(1)} + \delta^2\,\phi^{(2)} + ..., \tag{9}$$

with $\Phi^{\mathcal{I}}(t, x_i, X_i)$ which represents either $P^{\mathcal{I}}$ or $U_i^{\mathcal{I}}$; keeping in mind that these inner variables are function of both microscopic and macroscopic spatial coordinates, the chain rule $\dfrac{\partial}{\partial x_i} \rightarrow \dfrac{\partial}{\partial x_i} + \delta\dfrac{\partial}{\partial X_i}$ must be adopted when expressing spatial derivatives.

2.2 The microscopic model

In the model we treat the microscopic Reynolds number as an independent parameter, ignoring in Eq. (7b) the fact that Re_{inner} can be written as the product of δ times ℓ^+. This is similar in spirit to the procedure adopted when analyzing the linear stability of slowly spatially evolving flows, and a brief digression is in order. The Orr-Sommerfeld equation that describes the stability of, e.g., the Blasius boundary layer is the leading order result of a multiple-scale expansion in terms of a small parameter, ratio of the length scale of the wave to the scale of evolution of the base state [30–34]. This small parameter is related to the inverse of the Reynolds number which appears in the Orr-Sommerfeld equation, but such a relation is conveniently ignored. If it were not, the leading order system would consist in a differential equation of reduced order (the Rayleigh equation) not uniformly valid across the boundary layer, which would require a complex near-wall multi-deck treatment [35]. It is by now accepted that it is convenient and accurate to solve the Orr-Sommerfeld problem for boundary layers, lifting to lower order what are, formally, higher order terms, to ascertain the modal stability of the weakly non-parallel base flow; this produces good results for growth rates and frequencies even without computing higher order corrections.

We operate with the same logic in the present, different, context; since it has been argued in Sect. 2.1 that convective terms are non-negligible when h^+ and ℓ^+ exceed a few viscous units, we allow advective effects in the equations for the inner problem, which we write at leading order as follows:

$$\begin{aligned} &\frac{\partial u_i^{(0)}}{\partial x_i} = 0, \\ &\delta\ell^+\left(\frac{\partial u_i^{(0)}}{\partial t} + u_j^{(0)}\frac{\partial u_i^{(0)}}{\partial x_j}\right) + \frac{\partial p^{(0)}}{\partial x_i} - \frac{\partial^2 u_i^{(0)}}{\partial x_j^2} = 0. \end{aligned} \tag{10}$$

Should we set the product $\delta\ell^+$ to zero, we would recover the Stokes-like systems already solved by Bottaro and Naqvi [20]. Equations (10) define the microscopic problems to be solved numerically in the representative elementary volume (*REV*) of Fig. 1, subject to periodicity at the boundaries normal to the surface in $y = 0$ plus no-slip at the impermeable wall, situated in $y = y_{wall}$. The conditions to be enforced at $y \rightarrow \infty$ deserve careful inspection, since they will eventually yield the macroscopic effective conditions at the virtual wall in $Y = 0$.

2.3 Inner-outer matching

Continuity of the fields across the interface between the $\cdot^{\mathcal{O}}$ and $\cdot^{\mathcal{I}}$ regions is obtained by matching velocity and traction vectors at a dividing surface. If y_∞ is the inner vertical coordinate of such a surface (cf. Fig. 1, right frame), the corresponding position in outer coordinates is $Y_\infty = \delta\, y_\infty$. In dimensionless form, after accounting for the normalization of inner and outer variables, matching means that:

$$\langle U_i^{\mathcal{I}}\rangle\big|_{y=y_\infty} = \frac{1}{\delta}\,U_i^{\mathcal{O}}(t, X, Y_\infty, Z), \tag{11-a}$$

$$\langle -P^{\mathcal{I}}\,\delta_{i2} + \frac{\partial U_2^{\mathcal{I}}}{\partial x_i} + \frac{\partial U_i^{\mathcal{I}}}{\partial y}\rangle\Big|_{y=y_\infty} = \mathcal{S}_{i2}(t, X, Y_\infty, Z), \tag{11-b}$$

with δ_{ij} the Kronecker index and $\mathcal{S}_{i2} = \boldsymbol{\sigma} \cdot \boldsymbol{e}_2 = -P^{\mathcal{O}}\delta_{i2} + \frac{\partial U_2^{\mathcal{O}}}{\partial X_i} + \frac{\partial U_i^{\mathcal{O}}}{\partial Y}$ the outer traction vector, $\boldsymbol{\sigma}$ being the stress tensor. The symbol $\langle\cdot\rangle$ denotes surface averaging over x and z, across the microscopic *REV*, at any given y. Condition (11-a) can be further modified to eventually yield the macroscopic velocity at the virtual wall, by Taylor expanding the outer variables around $Y = 0$, i.e.

$$U_i^{\mathcal{O}}(t, X, Y_\infty, Z) = U_i^{\mathcal{O}}(t, X, 0, Z) + \delta\, y_\infty \frac{\partial U_i^{\mathcal{O}}}{\partial Y}\bigg|_{Y=0} + \delta^2 \frac{y_\infty^2}{2} \frac{\partial^2 U_i^{\mathcal{O}}}{\partial Y^2}\bigg|_{Y=0} + ..., \tag{12-a}$$

eventually leading to

$$U_i^{\mathcal{O}}(t, X, 0, Z) = \delta\left(\langle u_i^{(0)} \rangle\big|_{y=y_\infty} - y_\infty \frac{\partial U_i^{\mathcal{O}}}{\partial Y}\bigg|_{Y=0} \right) + \delta^2 \left(\langle u_i^{(1)} \rangle\big|_{y=y_\infty} - \frac{y_\infty^2}{2} \frac{\partial^2 U_i^{\mathcal{O}}}{\partial Y^2}\bigg|_{Y=0} \right) + ... \tag{12-b}$$

The matching condition on the stress at leading order in δ is

$$\langle -p^{(0)}\,\delta_{i2} + \frac{\partial u_2^{(0)}}{\partial x_i} + \frac{\partial u_i^{(0)}}{\partial y} \rangle\bigg|_{y=y_\infty} = \mathcal{S}_{i2}\big|_{Y=Y_\infty}. \tag{13-a}$$

The microscopic problem to be solved in the *REV* is thus formed by Eq. (10) with no-slip conditions at the wall, periodicity along x and z, plus condition (13a) at y_∞. The averaged Eq. (13a) cannot, however, be enforced as is; it can be relaxed, on the assumption that y_∞ is sufficiently far from y_{wall} for the order zero field to become invariant in x and z. In this case the boundary condition becomes:

$$-p^{(0)}\,\delta_{i2} + \frac{\partial u_2^{(0)}}{\partial x_i} + \frac{\partial u_i^{(0)}}{\partial y}\bigg|_{y=y_\infty} = \mathcal{S}_{i2}\big|_{Y=Y_\infty}. \tag{13-b}$$

2.4 Adjoint homogenization

The adjoint homogenization procedure [14] relies on the introduction of an inner product between two functions a and b defined over the *REV*. Here we choose the following simple definition of the inner product:

$$\int_{y_{wall}}^{y_\infty} \langle\, a\, b \,\rangle \,\mathrm{d}y. \tag{14}$$

We take the inner product of the continuity equation in (10) with the test vector $p_j^\dagger$ and subtract this from the inner product of the test tensor $u_{ji}^\dagger$ with the momentum equation, to obtain

$$\begin{aligned} 0 &= \int_{y_{wall}}^{y_\infty} \langle\, p_j^\dagger \frac{\partial u_i^{(0)}}{\partial x_i} - u_{ji}^\dagger \left[\delta\ell^+ \left(\frac{\partial u_i^{(0)}}{\partial t} + u_k^{(0)} \frac{\partial u_i^{(0)}}{\partial x_k} \right) + \frac{\partial p^{(0)}}{\partial x_i} - \frac{\partial^2 u_i^{(0)}}{\partial x_k^2} \right] \rangle\, \mathrm{d}y \\ &= \int_{y_{wall}}^{y_\infty} \langle\, \frac{\partial u_{ji}^\dagger}{\partial x_i} p^{(0)} + \left[\delta\ell^+ \left(\frac{\partial u_{ji}^\dagger}{\partial t} + u_k^{(0)} \frac{\partial u_{ji}^\dagger}{\partial x_k} \right) - \frac{\partial p_j^\dagger}{\partial x_i} + \frac{\partial^2 u_{ji}^\dagger}{\partial x_k^2} \right] u_i^{(0)} \rangle\, \mathrm{d}y \\ &\quad - \frac{\mathrm{d}}{\mathrm{d}t} \int_{y_{wall}}^{y_\infty} \langle\, u_{ji}^\dagger u_i^{(0)} \,\rangle\, \mathrm{d}y + \}\}\text{boundary termsε}. \end{aligned} \tag{15}$$

We impose that the test functions $u_{ji}^\dagger$ and $p_j^\dagger$ are solutions of

$$\frac{\partial u_{ji}^\dagger}{\partial x_i} = 0, \qquad -\delta\ell^+ \left(\frac{\partial u_{ji}^\dagger}{\partial t} + u_k^{(0)} \frac{\partial u_{ji}^\dagger}{\partial x_k} \right) = -\frac{\partial p_j^\dagger}{\partial x_i} + \frac{\partial^2 u_{ji}^\dagger}{\partial x_k^2}, \tag{16}$$

with the normalizing constraint that the term $\int_{y_{wall}}^{y_\infty} \langle\, u_{ji}^\dagger\, u_i^{(0)} \,\rangle \mathrm{d}y$ is time-invariant [36]. System (16), which depends on the direct velocity at leading order, $u_k^{(0)}$, permits, in principle, to retrieve an adjoint field $(p_j^\dagger, u_{ji}^\dagger)$. The equations–despite looking similar to the Navier–Stokes equations—are well-posed only when integrated backwards in time [36]. The boundary conditions for the adjoint problem must be chosen also by examining carefully the—so far unspecified—"boundary terms" in (15), which arise from integration by parts. Like in the case of the direct field, we impose that the adjoint variables are periodic along x and z; furthermore, we set $u_{ji}^\dagger = 0$ at $y = y_{wall}$. Then, the "boundary terms" lead to the following condition at y_∞:

$$\langle\, u_i^{(0)} \left(-p_j^\dagger \delta_{i2} + \frac{\partial u_{ji}^\dagger}{\partial x_2} \right) \rangle \Big|_{y_\infty} = \langle\, u_{ji}^\dagger \left(-p^{(0)} \delta_{i2} + \frac{\partial u_i^{(0)}}{\partial x_2} - \delta\ell^+ u_i^{(0)}\, u_2^{(0)} \right) \rangle \Big|_{y_\infty} . \tag{17}$$

At this point we set the outer boundary condition for the adjoint problem:

$$-p_j^\dagger \delta_{i2} + \frac{\partial u_{ji}^\dagger}{\partial x_2}\Big|_{y_\infty} = \delta_{ji}, \tag{18}$$

for the adjoint problem to be formally closed. Equation (17) yields the (x, z)–averaged value of the leading order microscopic velocity at y_∞:

$$\langle\, u_j^{(0)} \,\rangle \Big|_{y_\infty} = \langle\, u_{ji}^\dagger \left(-p^{(0)} \delta_{i2} + \frac{\partial u_i^{(0)}}{\partial x_2} - \delta\ell^+ u_i^{(0)}\, u_2^{(0)} \right) \rangle \Big|_{y_\infty} . \tag{19}$$

The wall being impermeable, at each instant of time it is $\langle\, u_2^{(0)} \,\rangle = 0$ for any value of y; if, as argued before, the leading order fields are assumed to be invariant along x and z on horizontal *REV* planes sufficiently far from the wall, then it is the local wall-normal velocity, $u_2^{(0)}$, which vanishes. This is consistent with Stokes-based calculations of the problem [14, 19, 20, 37] which have shown that the first non-zero transpiration term at the fictitious wall is $u_2^{(1)}$. On this basis, the equation above can be re-written as

$$\langle\, u_j^{(0)} \,\rangle \Big|_{y_\infty} = \langle\, u_{ji}^\dagger \,\rangle \Big|_{y_\infty} \left(-p^{(0)} \delta_{i2} + \frac{\partial u_i^{(0)}}{\partial x_2} + \frac{\partial u_2^{(0)}}{\partial x_i} \right) \Big|_{y_\infty} = \langle\, u_{ji}^\dagger \,\rangle \Big|_{y_\infty} S_{i2}\big|_{Y_\infty}, \tag{20}$$

on account of (13-b). Since $S_{i2}\big|_{Y_\infty}$ is the only forcing term of the direct problem, we could have immediately posed the ansatz commonly employed in homogenization [38] that

$$u_j^{(0)} = u_{ji}^\dagger S_{i2}\big|_{Y_\infty} \quad \text{and} \quad p^{(0)} = p_i^\dagger S_{i2}\big|_{Y_\infty} + P_0, \tag{21}$$

with P_0 an integration constant. Clearly, the result embodied by (20) is consistent with ansatz (21).

In the Stokes approximation ($Re_{inner} = \delta\ell^+ = 0$), invariance of the riblet geometry along x allows to treat the problem as two-dimensional in the (y, z) plane, with Eq. (16) reducing to an uncoupled Stokes-Laplace pair [9]. Numerical solutions can be easily conducted in the creeping flow limit, using the freefem++ solver [39], with piecewise P_2 continuous finite elements (except for $p_j^\dagger$ which is discretized with continuous piecewise-linear elements) on an unstructured grid composed by up to 200 000 triangular elements in the domain, with refinement near the solid boundary, to guarantee grid-converged solutions. For uniqueness a condition must also be imposed on $p_j^\dagger$: in our case, the integral of $p_j^\dagger$ on the domain is forced to vanish. When equilateral

Table 1 Non-zero auxiliary fields' values at the upper boundary of the *REV* for equilateral triangular riblets in the Stokes approximation

Re_{inner}	$u_{11}^\dagger\big\vert_{y_\infty=4}$	$u_{11}^\dagger\big\vert_{y_\infty=5}$	$u_{11}^\dagger\big\vert_{y_\infty=6}$	$u_{11}^\dagger\big\vert_{y_\infty=7}$	$u_{33}^\dagger\big\vert_{y_\infty=4}$	$u_{33}^\dagger\big\vert_{y_\infty=5}$	$u_{33}^\dagger\big\vert_{y_\infty=6}$	$u_{33}^\dagger\big\vert_{y_\infty=7}$
0	4.170660	5.170675	6.170678	7.170673	4.080549	5.080515	6.080529	7.080513

The values of $u_{11}^\dagger$ and $u_{33}^\dagger$ are uniform at each y_∞ indicated, differing from one spanwise position to any other one only in the sixth significant digit (after subtracting the corresponding value of y_∞ to retrieve λ_x and λ_z); the numbers reported are obtained through z-averaging at each $y = y_\infty$

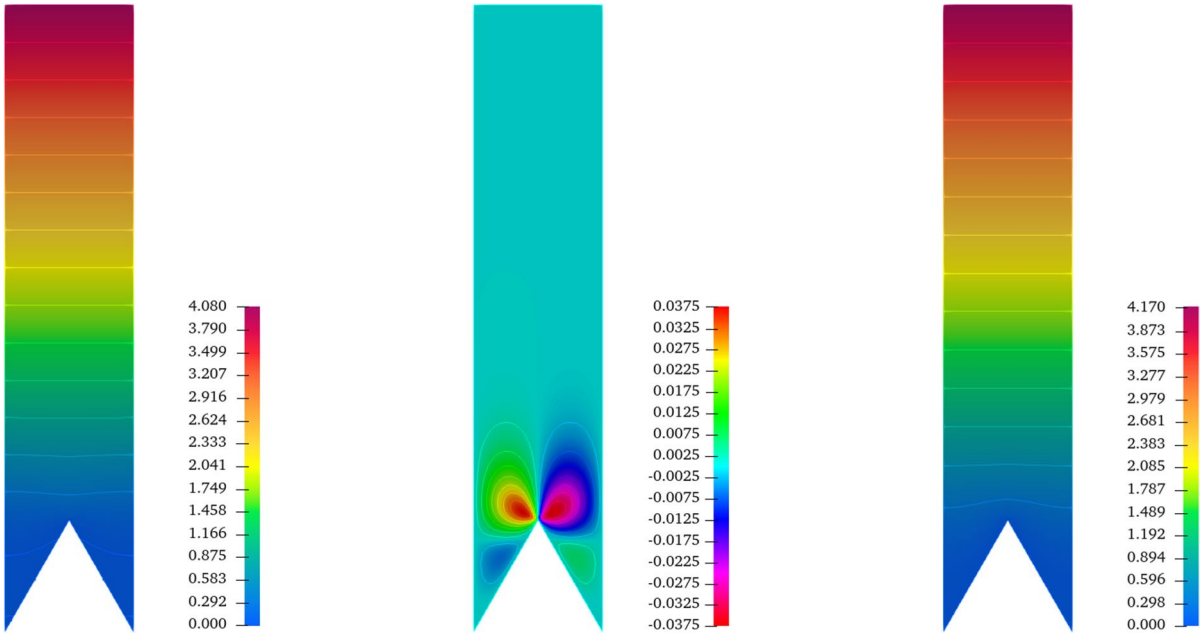

Fig. 2 Some steady auxiliary fields for equilateral triangular riblets. From left to right, isocontours of $u^\dagger_{33}$, $u^\dagger_{23}$ and $u^\dagger_{11}$

triangular riblets infinitely elongated in x are considered, the numerical solution of the problem yields the results reported in Table 1 and displayed in Fig. 2. The fields of the dagger variables are also called *auxiliary fields*. The values reported are uniform over the surface in y_∞, i.e. $\langle u^\dagger_{11}\rangle\big|_{y_\infty} = u^\dagger_{11}\big|_{y_\infty}$ and $\langle u^\dagger_{33}\rangle\big|_{y_\infty} = u^\dagger_{33}\big|_{y_\infty}$. All other values of $u^\dagger_{ji}$ go to zero at the upper boundary of the domain, provided y_∞ exceeds about 2.

With the above results, Eq. (20) reduces to:

$$\langle\, u_1^{(0)}\,\rangle\Big|_{y_\infty} = u_1^{(0)}\Big|_{y_\infty} = u^\dagger_{11}\Big|_{y_\infty}\, S_{12}\big|_{Y_\infty}, \tag{22-a}$$

$$\langle\, u_2^{(0)}\,\rangle\Big|_{y_\infty} = u_2^{(0)} = 0, \tag{22-b}$$

$$\langle\, u_3^{(0)}\,\rangle\Big|_{y_\infty} = u_3^{(0)}\Big|_{y_\infty} = u^\dagger_{33}\Big|_{y_\infty}\, S_{32}\big|_{Y_\infty}, \tag{22-c}$$

when y_∞ is sufficiently far from the tip of the ribs.

2.5 The transpiration velocity

We now go back to Eq. (12-b), and write out explicitly the expressions up to $\mathcal{O}(\delta)$ of the macroscopic boundary conditions to be enforced at $Y = 0$:

$$U_1^{\mathcal{O}}(t,X,0,Z) = \delta\left[u^\dagger_{11}\,\mathcal{S}_{12}\big|_{Y=\delta y_\infty} - y_\infty \frac{\partial U_1^{\mathcal{O}}}{\partial Y}\Big|_{Y=0}\right] + \mathcal{O}(\delta^2), \tag{23-a}$$

$$U_2^{\mathcal{O}}(t,X,0,Z) = \mathcal{O}(\delta^2), \tag{23-b}$$

$$U_3^{\mathcal{O}}(t,X,0,Z) = \delta\left[u^\dagger_{33}\,\mathcal{S}_{32}\big|_{Y=\delta y_\infty} - y_\infty \frac{\partial U_3^{\mathcal{O}}}{\partial Y}\Big|_{Y=0}\right] + \mathcal{O}(\delta^2). \tag{23-c}$$

The equations above for $U^{\mathcal{O}} = U_1^{\mathcal{O}}$ and $W^{\mathcal{O}} = U_3^{\mathcal{O}}$ can be further manipulated by Taylor expanding around $Y = 0$ all terms which contain $\mathcal{S}_{ij}$ evaluated at $Y = \delta y_\infty$. For example, we write $\mathcal{S}_{12}\big|_{Y=\delta y_\infty} = \mathcal{S}_{12}\big|_{Y=0} + \delta y_\infty \big(\partial \mathcal{S}_{12}/\partial Y\big)\big|_{Y=0} + \ldots$ and so on. Furthermore, to leading order in δ it is $S_{12}\big|_{Y=0} = (\partial U^{\mathcal{O}}/\partial Y)\big|_{Y=0}$ (and similarly for $S_{32}\big|_{Y=0}$), so that the slip conditions at the virtual wall become

$$U^{\mathcal{O}}(t,X,0,Z) = \delta\,\lambda_x \frac{\partial U^{\mathcal{O}}}{\partial Y}\Big|_{Y=0} + \mathcal{O}(\delta^2), \tag{24-a}$$

$$W^{\mathcal{O}}(t,X,0,Z) = \delta\,\lambda_z \frac{\partial W^{\mathcal{O}}}{\partial Y}\Big|_{Y=0} + \mathcal{O}(\delta^2), \tag{24-b}$$

with $\lambda_x = u_{11}^{\dagger}|_{y_\infty} - y_\infty$ and $\lambda_z = u_{33}^{\dagger}|_{y_\infty} - y_\infty$. Inspection of Table 1 demonstrates that the two slip lengths, λ_x and λ_z, are independent of the choice of y_∞. In particular, in the Stokes case for equilateral triangular riblets we have $\lambda_x = 0.1707$ and $\lambda_x = 0.0805$.

The transpiration speed $U_2^{\mathcal{O}} = V^{\mathcal{O}}$ at $Y = 0$ vanishes at leading order in terms of the expansion proposed because the real wall is impermeable, but it has been shown [14, 21] that neglecting vertical velocity fluctuations at the virtual wall can lead to serious errors in evaluating drag reduction/increase when modeling the presence of riblets which operate beyond the viscous regime. The significance of wall-normal velocity fluctuations for turbulent flows over rough surfaces has been highlighted in particular by Orlandi and co-workers [23–25].

We start by estimating $V^{\mathcal{O}}$ at $Y_\infty = \delta y_\infty$ with reference to the sketch on the right frame of Fig. 1. Equations (11-a) and (21) can be written to leading order for the case at hand as:

$$\left.\frac{\partial U_j^{\mathcal{O}}}{\partial Y}\right|_{Y_\infty} = \frac{\mathcal{C}_{jk}}{\delta}\, U_k^{\mathcal{O}}\big|_{Y_\infty}, \tag{25}$$

with j and k equal to 1 and 3, and the 2×2 diagonal matrix $\mathcal{C}$ defined as

$$\mathcal{C} = \begin{pmatrix} \dfrac{1}{u_{11}^{\dagger}|_{y_\infty}} & 0 \\ 0 & \dfrac{1}{u_{33}^{\dagger}|_{y_\infty}} \end{pmatrix}. \tag{26}$$

Expression (25) can be inserted into Eq. (21) to yield $u_j^{(0)} = \delta^{-1}\, u_{ji}^{\dagger}\, \mathcal{C}_{ik}\, U_k^{\mathcal{O}}\big|_{Y_\infty}$, with the index i which can also take only the values 1 and 3. As shown in reference [14], on account of continuity the order δ microscopic y-velocity component at the upper edge of the *REV* is

$$u_2^{(1)}|_{y_\infty} = v^{(1)}|_{y_\infty} = -\frac{\partial}{\partial x_i}\int_{y_{wall}}^{y_\infty} u_i^{(1)}\, dy - \frac{\partial}{\partial X_i}\int_{y_{wall}}^{y_\infty} u_i^{(0)}\, dy, \tag{27}$$

with the index i, again, equal to 1 and 3. Integrating in z from 0 to 1 gives

$$\begin{aligned}\int_0^1 v^{(1)}|_{y_\infty}\, dz &= -\frac{\partial}{\partial X_i}\int_{y_{wall}}^{y_\infty}\int_0^1 u_i^{(0)}\, dz\, dy \\ &= -\delta^{-1}\left[\int_{y_{wall}}^{y_\infty}\int_0^1 u_{ij}^{\dagger}\, dz\, dy\right]\mathcal{C}_{jk}\left.\frac{\partial U_k^{\mathcal{O}}}{\partial X_i}\right|_{Y_\infty},\end{aligned} \tag{28}$$

so that the macroscopic transpiration velocity at Y_∞ is

$$\begin{aligned}V^{\mathcal{O}}|_{Y_\infty} &= \delta^2\int_0^1 v^{(1)}|_{y_\infty}\, dz + \mathcal{O}(\delta^3) \\ &= -\,\delta\, m_{ik}\left.\frac{\partial U_k^{\mathcal{O}}}{\partial X_i}\right|_{Y_\infty} + \mathcal{O}(\delta^3).\end{aligned} \tag{29}$$

with $m_{ik} = \left[\int_{y_{wall}}^{y_\infty}\int_0^1 u_{ij}^{\dagger}\, dz\, dy\right]\mathcal{C}_{jk}$. In the present setting the matrix of components m_{ik} is diagonal, with

$$\begin{aligned}m_{11} &= \frac{1}{u_{11}^{\dagger}|_{y_\infty}}\int_{y_{wall}}^{y_\infty}\int_0^1 u_{11}^{\dagger}\, dz\, dy, \qquad m_{33} \\ &= \frac{1}{u_{33}^{\dagger}|_{y_\infty}}\int_{y_{wall}}^{y_\infty}\int_0^1 u_{33}^{\dagger}\, dz\, dy.\end{aligned} \tag{30}$$

The effective condition (29) must now be transferred to $Y = 0$; this is easily accomplished by expanding $V^{\mathcal{O}}$ around $Y = 0$, i.e.

$$\begin{aligned}&V^{\mathcal{O}}|_{Y_\infty} = V^{\mathcal{O}}|_{Y=0} + \delta y_\infty \left.\frac{\partial V^{\mathcal{O}}}{\partial Y}\right|_{Y=0} \\ &+ \delta^2\frac{y_\infty^2}{2}\left.\frac{\partial^2 V^{\mathcal{O}}}{\partial Y^2}\right|_{Y=0} + \mathcal{O}(\delta^3) = \\ &V^{\mathcal{O}}|_{Y=0} + \delta y_\infty\left.\left[-\frac{\partial U^{\mathcal{O}}}{\partial X} - \frac{\partial W^{\mathcal{O}}}{\partial Z}\right]\right|_{Y=0} \\ &+ \delta^2\frac{y_\infty^2}{2}\frac{\partial}{\partial Y}\left.\left[-\frac{\partial U^{\mathcal{O}}}{\partial X} - \frac{\partial W^{\mathcal{O}}}{\partial Z}\right]\right|_{Y=0} + \mathcal{O}(\delta^3) = \\ &V^{\mathcal{O}}|_{Y=0} - \delta y_\infty\left.\left\{\frac{\partial}{\partial X}\left[\delta\lambda_x\frac{\partial U^{\mathcal{O}}}{\partial Y}\right] + \frac{\partial}{\partial Z}\left[\delta\lambda_z\frac{\partial W^{\mathcal{O}}}{\partial Y}\right]\right\}\right|_{Y=0} \\ &- \delta^2\frac{y_\infty^2}{2}\left.\left[\frac{\partial^2 U^{\mathcal{O}}}{\partial Y\partial X} + \frac{\partial^2 W^{\mathcal{O}}}{\partial Y\partial Z}\right]\right|_{Y=0} + \mathcal{O}(\delta^3).\end{aligned} \tag{31}$$

Expanding in a similar manner the term on right hand side of Eq. (29) it is obtained:

$$V^{\mathcal{O}}\big|_{Y_\infty} = -\delta\, m_{11}\left[\frac{\partial U^{\mathcal{O}}}{\partial X} + \delta y_\infty \frac{\partial^2 U^{\mathcal{O}}}{\partial Y \partial X}\right]\Bigg|_{Y=0} - \delta\, m_{33}\left[\frac{\partial W^{\mathcal{O}}}{\partial Z} + \delta y_\infty \frac{\partial^2 W^{\mathcal{O}}}{\partial Y \partial Z}\right]\Bigg|_{Y=0} + \mathcal{O}(\delta^3) = - \delta\, m_{11}\left\{\frac{\partial}{\partial X}\left[\delta\lambda_x \frac{\partial U^{\mathcal{O}}}{\partial Y}\right] + \delta y_\infty \frac{\partial^2 U^{\mathcal{O}}}{\partial Y \partial X}\right\}\Bigg|_{Y=0} - \delta\, m_{33}\left[\frac{\partial}{\partial Z}\left[\delta\lambda_z \frac{\partial W^{\mathcal{O}}}{\partial Y}\right] + \delta y_\infty \frac{\partial^2 W^{\mathcal{O}}}{\partial Y \partial Z}\right]\Bigg|_{Y=0} + \mathcal{O}(\delta^3). \tag{32}$$

Putting together (31) and (32) it is finally found:

$$V^{\mathcal{O}}(t, X, 0, Z) = -\delta^2\left[\mathcal{K}^{itf}_{xy}\frac{\partial^2 U^{\mathcal{O}}}{\partial Y \partial X} + \mathcal{K}^{itf}_{zy}\frac{\partial^2 W^{\mathcal{O}}}{\partial Y \partial Z}\right]\Bigg|_{Y=0} + \mathcal{O}(\delta^3), \tag{33}$$

with $\mathcal{K}^{itf}_{xy} = [m_{11}(y_\infty + \lambda_x) - y_\infty \lambda_x - y_\infty^2/2]$ and $\mathcal{K}^{itf}_{zy} = [m_{33}(y_\infty + \lambda_z) - y_\infty \lambda_z - y_\infty^2/2]$ playing the role of interface permeability coefficients [14, 20]. Another form, more convenient for computational purposes, of (33) can be found by using (24-a) and (24-b), and this is:

$$V^{\mathcal{O}}(t, X, 0, Z) = -\delta\, n_{11}\frac{\partial U^{\mathcal{O}}}{\partial X}\Big|_{Y=0} - \delta\, n_{33}\frac{\partial W^{\mathcal{O}}}{\partial Z}\Big|_{Y=0} + \mathcal{O}(\delta^3), \tag{34}$$

with $n_{11} = \mathcal{K}^{itf}_{xy}/\lambda_x$ and $n_{33} = \mathcal{K}^{itf}_{zy}/\lambda_z$. It is important to stress the fact that n_{11} and n_{33}, just like the Navier slip coefficients λ_x and λ_z and the interface permeability coefficients, are independent of the choice of y_∞ of the *REV*. Boundary condition (34) at the effective surface in $Y = 0$, together with (24-a) and (24-b), allow the model in (7-a) for the macroscopic variables $(U^{\mathcal{O}}, V^{\mathcal{O}}, W^{\mathcal{O}}, P^{\mathcal{O}})$ to be closed.

The coefficients of interest are reported in Table 2 for the few riblets' shapes displayed in Fig. 3. The results are believed to be accurate up to the last significant digit reported. The parameter ℓ_g in the table is the square root of the groove cross-section A_g sketched in Fig. 1; it is a purely geometrical factor introduced by García-Mayoral and Jiménez [40] to capture both the influence of riblets' spacing and shape. In recent experimental and numerical works it has become customary to report drag reduction against ℓ_g^+, measured in viscous

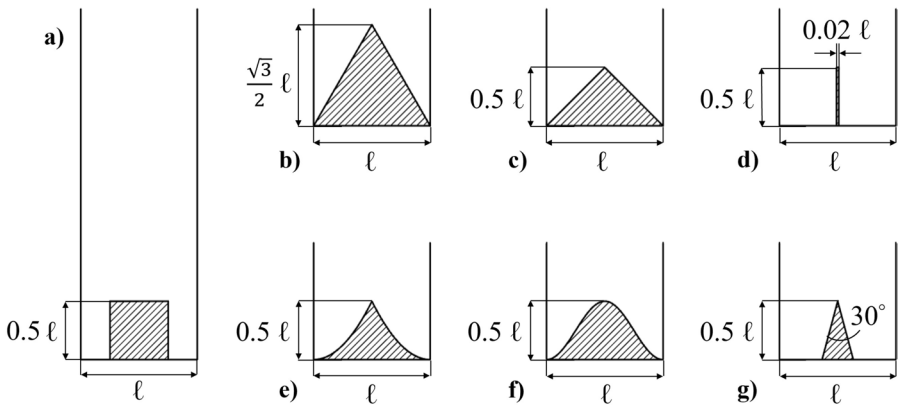

Fig. 3 Riblets' shapes: square **a**, equilateral triangle **b**, right triangle **c**, blade **d**, parabolic/scalloped **e**, cosine **f**, trapezoidal **g**

Table 2 Effective coefficients for the riblets' shapes in Fig. 3, in the Stokes limit

Riblets' shape	λ_x	λ_z	$\mathcal{K}^{itf}_{xy}$	$\mathcal{K}^{itf}_{zy}$	$\Delta\lambda = \lambda_x - \lambda_z$	ℓ_g/ℓ
Square	0.0415	0.0179	0.0058	0.0004	0.0236	0.5000
Equilateral triangle	0.1707	0.0805	0.0282	0.0058	0.0901	0.7530
Right triangle	0.1397	0.0779	0.0168	0.0058	0.0618	0.5000
Blade	0.1915	0.0784	0.0379	0.0046	0.1131	0.7000
Parabolic/scalloped	0.1699	0.0804	0.0259	0.0060	0.0894	0.5773
Cosine	0.1141	0.0638	0.0140	0.0042	0.0503	0.4262
Trapezoidal	0.1912	0.0820	0.0348	0.0054	0.1091	0.6830

units, since the data appear to collapse better onto a single curve for a variety of conventional riblet geometries, with clearly defined, open grooves fully exposed to the outer flow.

Two things must be noticed. The first is that λ_z, which defines the origin of the crossflow motion below the virtual plane, is significantly smaller than the pattern periodicity. The average value of λ_z for the seven cases examined is 0.0687, very close to α^{-1}, with $\alpha \approx 15$, supporting the scaling arguments of Sect. 2.1.

Second, skin-friction drag reduction is known to behave linearly with the riblets' periodicity for ℓ^+ of only up to a few viscous units [5]. This so-called *viscous regime* holds over a range smaller by a factor of about 2, cf. last column of Table 2, when observed in terms of ℓ_g^+. In this regime, we recall that Luchini [10] has shown that the reduction in skin friction coefficient with respect to the smooth-wall value is proportional to $\Delta\lambda^+ = \lambda_x^+ - \lambda_z^+$, according to Eq. (1), with μ_0 a constant close to one.

From Table 2 it can be ascertained that, at least in the viscous range, thinner riblets perform better; the best drag reduction is achieved by blade riblets, among the shapes considered, in agreement with Bechert et al. [5]. To properly assess what goes on for ℓ^+ beyond about 10, including values large enough for drag reduction to turn into drag increase [40], the effect of advection and transpiration through the grooves must be accounted for.

2.6 A vortex model for advection

We now go back to Eq. (16) and approximate the advective term $-\delta\ell^+ \left(u_k^{(0)} \dfrac{\partial u_{ji}^\dagger}{\partial x_k} \right)$, considering that direct numerical simulations of turbulence over

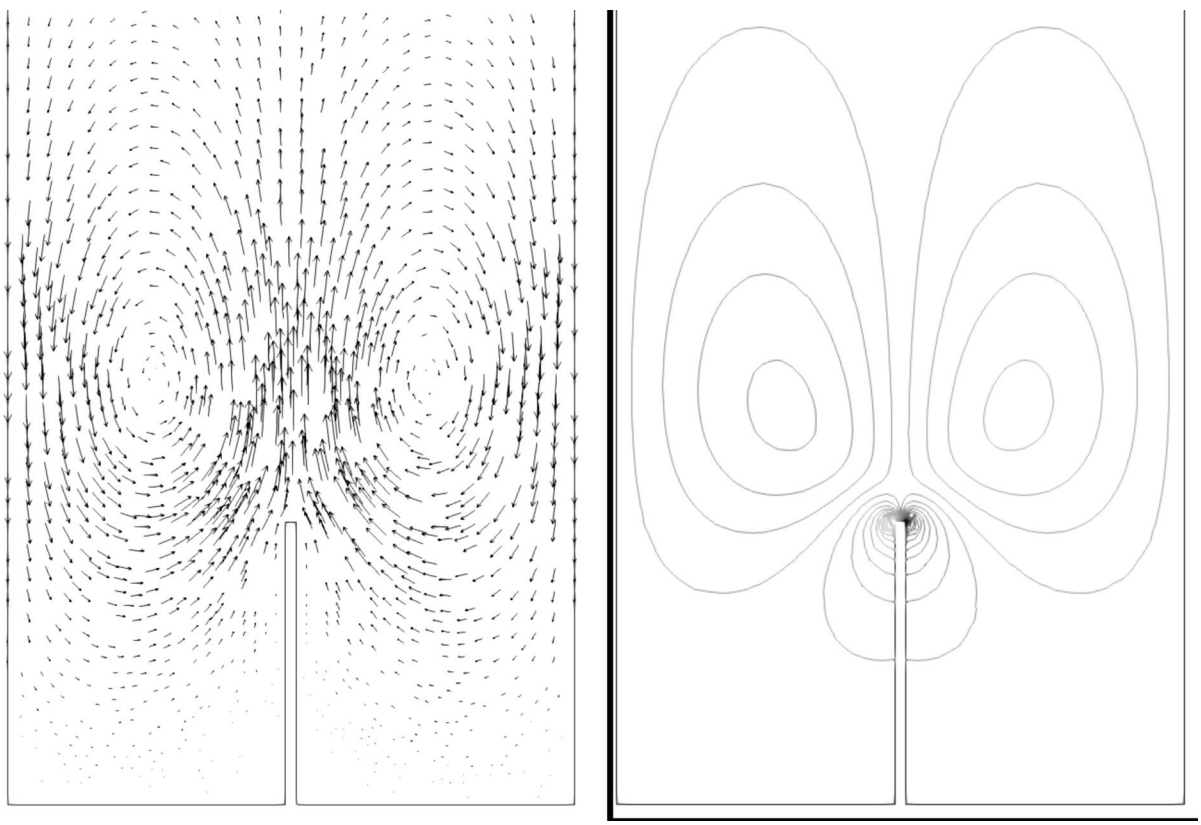

Fig. 4 Synthetic near-wall vortices for blade riblets ($\mathcal{P} = 160$), displayed via velocity vectors of the (v_V^+, w_V^+) field and contours of the streamwise vorticity, ω_x

riblets [13, 26, 41] have furnished indications of the flow structures that emerge in the proximity of individual grooves. In particular, ensemble-averaged results of the secondary flow by Modesti et al. [26] highlight the presence of a pair of counter-rotating vortices, symmetric about a vertical mid-line, with upwash above the riblet tip which increases in intensity with the increase of the spanwise periodicity. For example, for the case of trapezoidal riblets of height $h = \ell/2$ (like in our case), the largest upwash velocity, v^+ in viscous units attains the value of about 0.04 when $\ell^+ = 18$ and 0.15 when $\ell^+ = 36$ [26, 42]; as the spacing between neighboring riblets increases, the average downward secondary flow transports streamwise momentum into the groove more efficiently, yielding an increase in drag. However, even for $\ell^+ = 63$, the vortices are not lodged inside the grooves and tend to linger on top of them, with each vortex in the pair centered slightly above the riblet tip. The numerical simulations by Goldstein and Tuan [12] for scalloped, short riblets indicate that the streamwise vortex pair exhibits a maximum vertical velocity around 0.03 when $\ell^+ = 23$ and $h^+ = 8.7$, increasing to 0.12 when ℓ^+ reaches 62.8 (for $h^+ = 8.9$).

On the basis of the results above, we have decided to create a *synthetic* streamwise vortex pair, shown in Fig. 4 for the case of blade riblets, solution of a forced Stokes system with periodicity conditions at $z = 0$ and 1, no-slip at the walls, and with a velocity which dies out rapidly outside of the roughness sublayer, i.e. for $y^+ \gtrsim \ell^+$. It has been found convenient to build the vortex, of velocity components (v_V^+, w_V^+) in the $(y, z) = (x_2, x_3)$ plane, by forcing the equations for the "plus" variables with the $u_{ji}^\dagger$ fields computed from Eq. (16) with $\delta = 0$, i.e.:

$$\frac{\partial v_V^+}{\partial x_2} + \frac{\partial w_V^+}{\partial x_3} = 0, \quad -\frac{\partial p_V^+}{\partial x_2} + \frac{\partial^2 v_V^+}{\partial x_i^2} = \mathcal{P}\left[u_{j3}^\dagger \frac{\partial u_{23}^\dagger}{\partial x_j}\right],$$
$$-\frac{\partial p_V^+}{\partial x_3} + \frac{\partial^2 w_V^+}{\partial x_i^2} = \mathcal{P}\left[u_{j3}^\dagger \frac{\partial u_{33}^\dagger}{\partial x_j}\right], \tag{35}$$

with the indices i and j which take the values 2 and 3. The intensity of the vortex pair can be tuned by acting on the parameter $\mathcal{P}$. Clearly, this leaves a degree of arbitrariness in the definition of the vortex, while at the same time providing the necessary flexibility to calibrate the background (v_V^+, w_V^+) field to try and match available results. We have found that values of $\mathcal{P}$ in a neighborhood of 160 yield secondary flows of size and upwash velocity in the range of those quoted by Goldstein and Tuan [12], Endrikat [13] and Modesti et al. [26]. The vectors in Fig. 4 (left frame) highlight the shape of the vortex pair for the largest periodicity tested here ($\ell^+ = 40.6$) with a maximum vertical velocity equal to 0.11 (in plus units). The figure also displays isolines of the streamwise vorticity; the values of $\omega_x = \dfrac{\partial v_V^+}{\partial z^+} - \dfrac{\partial w_V^+}{\partial y^+}$ at the vortex centers are equal to ± 0.023.

If we now model the advective term in Eq. (16) by assuming that the $u_{ji}^\dagger$ field develops on top of a streamwise-invariant mean field plus a synthetic vortex pair which depends on only y and z, then

$$-\delta\ell^+\left(u_k^{(0)}\frac{\partial u_{ji}^\dagger}{\partial x_k}\right) = -\ell^+\left(v_V^+\frac{\partial u_{ji}^\dagger}{\partial y} + w_V^+\frac{\partial u_{ji}^\dagger}{\partial z}\right), \tag{36}$$

on account of the velocity scaling in Eq. (6-b). The term has a negligible contribution for ℓ^+ equal to a few units (where the viscous approximation holds), but becomes significant for larger periodicity. Once the new $u_{ji}^\dagger$ fields are computed, the slip and interface permeability coefficients are obtained exactly in the same manner as before, cf. Sect. 2.5. Some results are

Table 3 Effective coefficients for blade riblets, Fig. 3d, with the model for advection ($\mathcal{P} = 160$)

ℓ^+	ℓ_g^+	$\max(v_V^+)$	$\lvert\omega_x\rvert_{vortex\ center}$	λ_x	λ_z	$\mathcal{K}_{xy}^{itf}$	$\mathcal{K}_{zy}^{itf}$	$\Delta\lambda$
Stokes	–	–	–	0.1915	0.0784	0.0379	0.0046	0.1131
17.7	12.4	0.11	0.052	0.1730	0.0766	0.0400	0.0076	0.0964
27.9	19.5	0.11	0.034	0.1473	0.0740	0.0468	0.0097	0.0733
40.6	28.4	0.11	0.023	0.1038	0.0690	0.0599	0.0126	0.0348

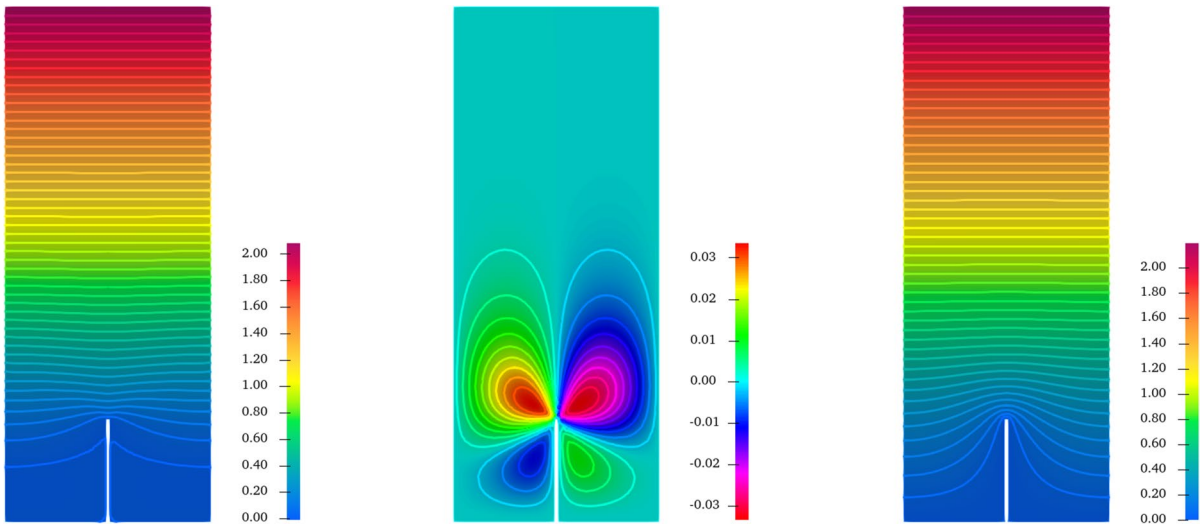

Fig. 5 Some auxiliary fields in the Stokes limit, in the vicinity of blade riblets. From left to right, isocontours of $u^{\dagger}_{33}$, $u^{\dagger}_{23}$ and $u^{\dagger}_{11}$

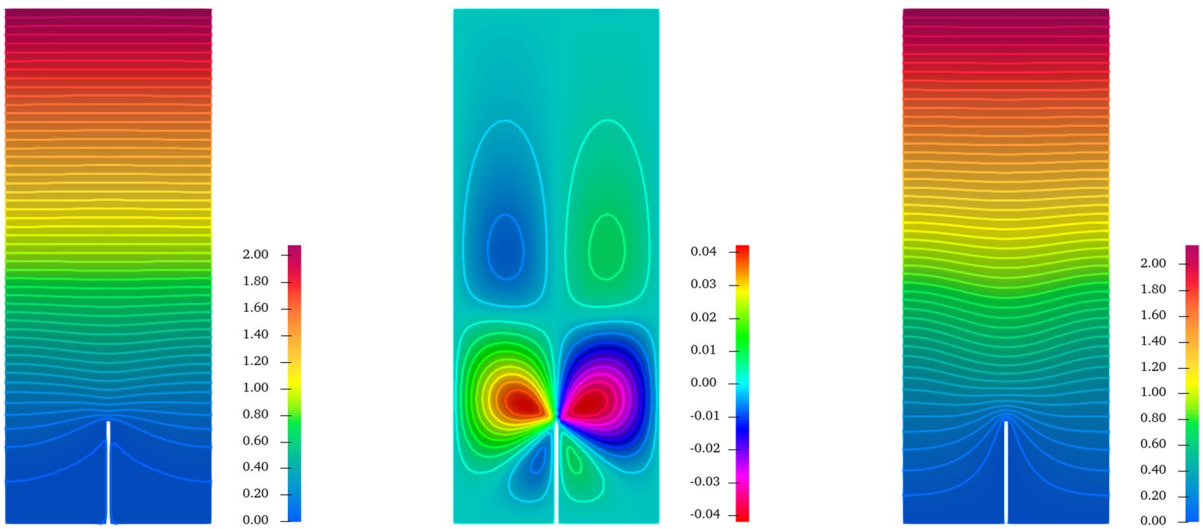

Fig. 6 Same as Fig. 5 for $\ell^+ = 27.9$ using the advection model ($\mathcal{P} = 160$)

proposed in Table 3 for the case of blade riblets. It is interesting to observe the rapid decrease of the streamwise slip coefficient, λ_x, with the increase of ℓ^+, and the slower decrease of λ_z. The drop in the value of $\Delta\lambda$ with ℓ^+ is indicative of performance deterioration (cf. Eq. 1).

Figures 5 and 6 report some relevant auxiliary fields for blade riblets without and with the advection vortex model. Differences between the fields in the figures do not seem particularly significant, aside perhaps for the presence of two extra coherent regions above the ribs in the isocontours of $u^{\dagger}_{23}$, a signature of the presence of the vortex pair. Despite such mild qualitative differences, λ_x decreases significantly compared to the creeping flow approximation, while λ_z experiences a milder reduction (cf. Table 3). The trend of λ_x with respect to the Stokes' value seems in contrast with the texture-resolving direct numerical

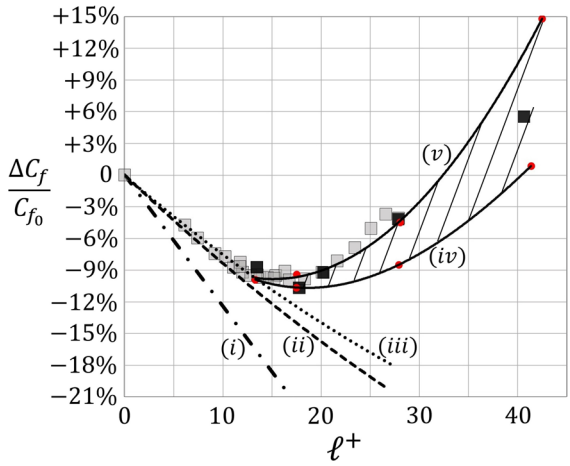

Fig. 7 Drag reduction versus spacing for blade riblets. The grey symbols correspond to experimental data by Bechert et al. [5] for bulk Reynolds number, based on average channel velocity and half the channel height, in the range 4000–15000, while the black symbols are direct numerical simulation results by El-Samni et al. [44] (at $Re_{bulk} = 2821$, $Re_\tau = 180$) which account for the microscopic geometry of the wall textures. The dot-dashed line (i) is the viscous, analytical solution given in Eq. (1) with $\mu_0 = 1$. The dashed line (ii) corresponds to our results obtained by direct simulations using only the Stokes slip coefficients for the tangential velocity components, without transpiration. The dotted line (iii) is obtained by using the Stokes slip coefficients plus transpiration at the fictitious wall, via Eq. (34); such a line almost coincides with results obtained using the model by Wong et al. [22]. The shaded region encloses direct numerical simulation results which could be obtained by the present slip-transpiration-vortex model. The two boundaries of this region, drawn with solid lines (iv) and (v), pertain, respectively, to $\mathcal{P} = 140$ and 180, with red symbols corresponding to the simulations conducted

simulations of turbulence over ribleted surfaces by Wong et al. [22] (cf. their Fig. 7a), which display a mild increase of the distance of the virtual origin of the mean streamwise velocity component from the crests of the riblets, past $\ell_g^+ \approx 15$. This matter deserves further, future scrutiny.

As opposed to the case of the slip lengths, the interface permeability components increase significantly with respect to the creeping flow case; $\mathcal{K}_{xy}^{itf}$ has grown by 58% (when comparing the Stokes' value to that at $\ell^+ = 40.6$) and $\mathcal{K}_{zy}^{itf}$ has more than doubled. The growth in the interface permeability coefficients is correlated to enhanced wall transpiration at the virtual wall in $Y = 0$. This effect can be quantified with the help of direct simulations of the turbulent motion over the modelled surface.

Before proceeding further, we come back to the very recent approach by Wong et al. [22], which bears some similarities to the present one. They have modeled the near-wall flow by solving the Stokes equations in a spanwise-periodic domain encompassing multiple riblets, forcing the motion at the upper y-boundary of their two-dimensional domain with cross-flow velocity components of prescribed wavelength and amplitude, to mimic the effect of outer, smooth-wall-like turbulence. The model, dubbed *viscous vortex model*, was used in particular to predict the transverse slip length, and assess how it varied as a consequence of near-wall upwash/downwash motion, for riblets of increasing periodicity. Upon assuming that the origin of the mean streamwise flow does not vanish, Wong and co-workers were able to estimate the roughness function, ΔU^+, and obtain an acceptable agreement with experimental results and texture-resolving direct simulations for a variety of riblets' shapes, up to $\ell_g^+ \approx 10.7$, i.e. the position of maximum drag reduction. For the case of blade riblets, examined here, the model by Wong et al. [22] works until $\ell^+ \approx 15$ (cf. their Fig. 17, frame k); beyond this values it predicts a monotonic decrease in drag, at least in the range of riblets' pitch values considered. The failure of the model to capture the breakdown of the drag curve has been ascribed by the authors to the fact that the outer forcing field mimics smooth-wall-like turbulence and, as such, is unable to capture the rapid increase in near-wall Reynolds stress when ℓ_g^+ exceeds 10.7.

3 The macroscale problem

3.1 Problem description and numerical setup

Large-scale numerical simulations are conducted using both the Stokes coefficients and the coefficients in Table 3 for the case of blade riblets, to model the presence of microgrooves using the effective conditions (24-a), (24-b) and (34). They resemble those used by Gómez-de-Segura et al. [43], except for a notable difference; the condition used in ref. [43] for the transpiration velocity is (using our notations)

$$V^{\mathcal{O}}(t,X,0,Z) = \delta\,\lambda_y \left.\frac{\partial V^{\mathcal{O}}}{\partial Y}\right|_{Y=0} \tag{37}$$

and it coincides with Eq. (34) only for isotropic textures in the $(x,\ z)$-plane, i.e. when $\lambda_y = n_{11} = n_{33}$. Clearly, this is not the case of riblets.

We study the turbulent flow in a channel delimited from the top side by a smooth boundary and from the bottom side by a corrugated wall; this is similar to the case sketched in Fig. 1, yet the riblets considered here are thin blades of pitch ℓ, height $0.5\,\ell$, and thickness $0.02\,\ell$ (cf. Fig. 3d). The dimensions of the free-fluid region beyond the rims of the riblets (i.e. the computational domain of interest for the macroscopic simulations) are $L_X \times L_Y \times L_Z = 2\pi H \times 2H \times \pi H$, with H half the channel height. Given that the magnitude of the macroscopic pressure gradient driving the flow in the channel is $\mathcal{M} = |\Delta\hat{p}/L_X|$, a bulk stress $\tau_{\mathcal{M}} = \mathcal{M}H$ can be defined, and it can be proven from the momentum balance in the macroscopic domain that $\tau_{\mathcal{M}} = (\tau_{\mathcal{F}} + \tau_{\mathcal{T}})/2$, where $\tau_{\mathcal{F}}$ and $\tau_{\mathcal{T}}$ are the total shear stresses at the fictitious boundary $(\hat{y} = 0)$ and at the top, smooth wall $(\hat{y} = 2H)$, respectively. Correspondingly, we define a shear velocity $u_{\tau(\mathcal{M})} = \sqrt{\tau_{\mathcal{M}}/\rho}$ and a shear-velocity Reynolds number $Re_{\tau(\mathcal{M})} = \dfrac{\rho u_{\tau(\mathcal{M})} H}{\mu}$ with a fixed value of about 193 for all the simulations carried out. The riblet pitch is varied from one simulation to another such that different values of $\ell^+_{\mathcal{M}} = \dfrac{\rho u_{\tau(\mathcal{M})}\ell}{\mu}$ are considered, in particular $\ell^+_{\mathcal{M}} = (13.5, 17.7, 27.9, 40.6)$. The shear stress at the corrugated wall, τ_w, (i.e. the drag evaluated per unit plan area for the bottom physical surface) can be retrieved theoretically by applying momentum balance over the whole domain (macroscopic plus microscopic), yielding $\tau_w \approx (2\tau_{\mathcal{M}} - \tau_{\mathcal{T}}) + \tau_{\mathcal{M}}\dfrac{\ell}{2H} = \tau_{\mathcal{F}} + \tau_{\mathcal{M}}\dfrac{\ell}{2H}$, with the thickness of the thin blades neglected. To permit comparison with the reference data [44], the numerical results reported are normalized based on τ_w as given above. The pitch distance measured in viscous units, ℓ^+, is found to differ by less than 5% from $\ell^+_{\mathcal{M}}$. In terms of the half-channel height, the periodicity of the riblets is equal to $\ell = (0.070, 0.092, 0.144, 0.210)\,H$.

Direct numerical simulations of the macroscale problem are run using the Simcenter STAR-CCM+ finite-volume-based software. The grid resolution and the numerical procedure are the same as in references [21, 45]; in particular, the mesh is uniform in the streamwise and spanwise directions, while it is stretched gradually in the wall-normal direction departing from the upper and lower walls (thinnest layer) towards the centerline of the channel (thickest layer); the grid spacings in viscous units are $h_X^+ = 9.47, h_Z^+ = 6.32, h_Y^+|_{min} = 0.27, h_Y^+|_{max} = 9.25$. In brief, the convective fluxes are discretized using a third-order scheme formulated as a linear blend between *MUSCL* third-order upwind and a third-order central-differencing expression. A second-order implicit scheme is employed for temporal discretization with 20 internal iterations performed at each time step. The time step is set to $0.001H/u_{\tau(\mathcal{M})}$ for the maximum convective Courant-Friedrichs-Lewy (CFL) number to be maintained below 1. The averaging time, after the initial transient of the flow field in each simulation, is typically taken equal to $40\,H/u_{\tau(\mathcal{M})}$. Finally, it is important to highlight that, despite the presence of local transpiration velocities, the surface-integrated value of $V^{\mathcal{O}}$ at $Y = 0$ remains negligibly small, i.e. unlike the case of the porous interface treated by Ahmed and Bottaro [21], no correction is required here at the fictitious wall to satisfy conservation of mass.

3.2 Results and discussion

We first focus on the ability of the linear relation (1) and different homogenization-based models to predict the behavior of the skin-friction drag over blade riblets, by validating the results obtained against the reference experimental/numerical results by Bechert et al. [5] and El-Samni et al. [44], as presented in Fig. 7. It is clear from the figure that Eq. (1) with $\mu_0 = 1$ [10] provides inaccurate results even for vanishingly small riblets. Three different settings of the direct numerical simulations have been investigated, modifying the definition of the macroscopic velocity boundary conditions. The skin-friction coefficient is evaluated as $C_f = \dfrac{2\tau_w}{\rho\,(\hat{u}_{bulk})^2}$, with $\hat{u}_{bulk}$ the temporally and spatially averaged velocity over the whole

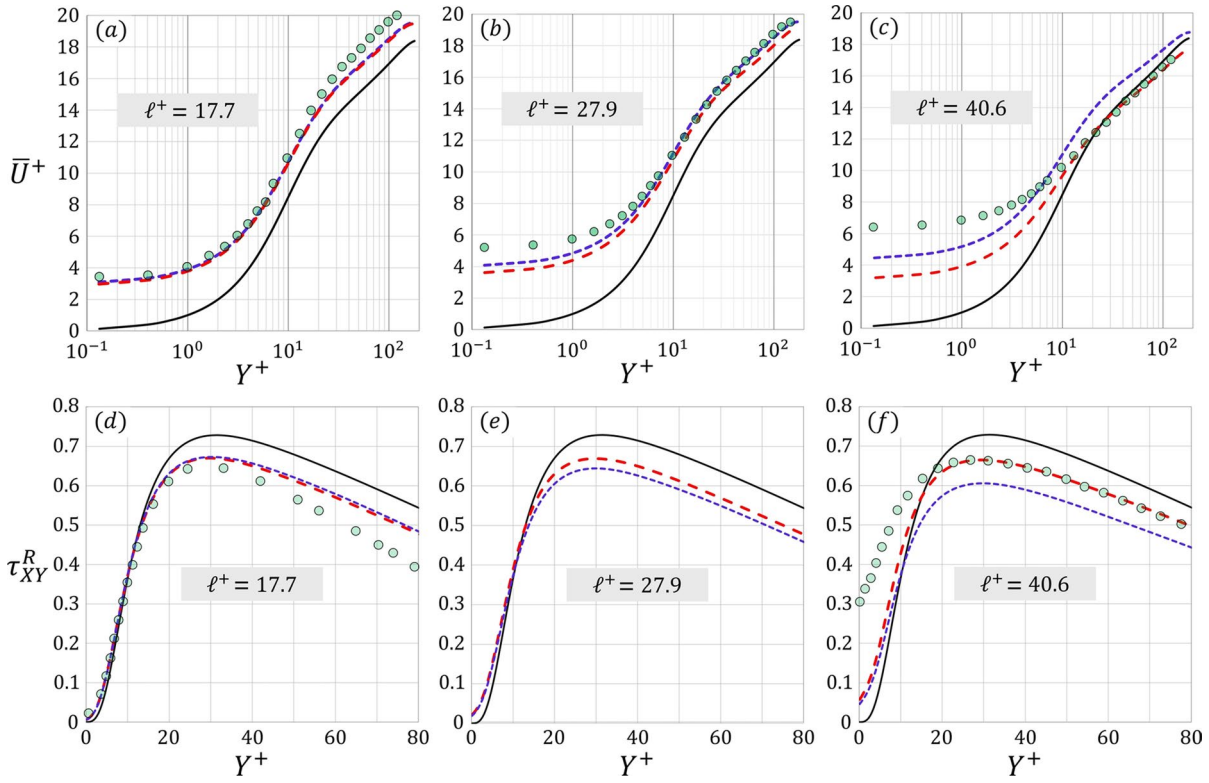

Fig. 8 Mean velocity (top row) and Reynolds stress as function of Y^+ for three values of ℓ^+. In each frame, the solid line reports the solution for the flow in a channel with two smooth walls, while blue and red dashed lines correspond to the results of the turbulent motion in a ribbed channel using, respectively, $\mathcal{P} = 140$ and 180 in the model. The available data from El-Samni et al. [44] are plotted with small circular symbols, after having matched the origin of the data in [44] to ours

channel (of total height equal to $2H + h$). Since the DNSs conducted are concerned with the average velocity in the free-fluid region only, a separate estimation of the average velocity in the riblet layer ($\hat{u}_R$) is needed for the evaluation of $\hat{u}_{bulk}$. From a theoretical perspective, the value of $\hat{u}_R$ is expected to be smaller than $\hat{u}_{slip}$ (the velocity at the fictitious interface) and larger than 0 (the velocity at the trough of the groove). An intermediate value of $\hat{u}_R \approx 0.5\,\hat{u}_{slip} \approx 0.5\,\lambda_x^+ u_\tau$ is adopted as an approximation in the present work. The transpiration-free model with Stokes macroscopic coefficients (dashed line) represents the simplest form of the boundary conditions, and its predictions appear to be valid only up to $\ell^+ \approx 10$. Incorporating the transpiration velocity (37) component permits a moderately wider validity range (up to $\ell^+ \approx 15$, dotted line). When advection is taken into account in the evaluation of the upscaled coefficients, employing the present vortex model, we are able to capture the parabolic shape of *DR* as function of ℓ^+. In this case, it is clear that the results increasingly depend on the vortex intensity as the riblets' spacing grows, and thus the choice of the forcing parameter $\mathcal{P}$ (cf. Eq. 35) becomes critical. Since our aim is not that of optimizing the agreement with previous experiments and simulations, but to develop and test practical boundary conditions which might apply to riblet configurations beyond the viscous regime, we have simply chosen values of $\mathcal{P}$ which provide, for the streamwise vortex pair that sits above the rib, intensities in the expected range [12, 13].

In Fig. 8, the results of our direct numerical simulations (with vortex-model-based effective coefficients) for the distributions of the mean velocity $\overline{U}^+$ and the Reynolds shear stress τ^R_{XY} in the free-fluid region next to the lower boundary are plotted and

compared against those in reference [44]. When ℓ^+ is approximately equal to 17.7 and 27.9 the agreement between the model results and the available texture-resolving data appears acceptable. Also, the model, with $\mathcal{P}$ set to 180, appears to accurately capture the logarithmic behavior of the mean velocity for $\ell^+ = 40.6$, a value which is far beyond the viscous range. The same applies also to the peak value of the Reynolds shear stress. Conversely, the present version of the model has a weakened ability to predict $\overline{U}^+$ and τ^R_{XY} at and in close vicinity of the corrugated surface with the increase of ℓ^+. A possible reason for the poor agreement between our results and those by El Samni et al. [44] near the surface when ℓ^+ is large, could be related to the issue of our slip lengths (and $\Delta\lambda$) decreasing with the increase of the riblets' periodicity (cf. Table 3 and related discussion in Sect. 2.6). Another possible explanation has been suggested to us by a referee, and is related to the resolution of the DNSs by El Samni et al. [44]. The referee pointed out to us that the number of grid points between neighboring riblets in [44] ranges from 6 to 16 for the three values of ℓ considered, and this might be marginally sufficient to resolve the dynamics of the fluid within adjacent corrugations.

4 Concluding remarks

A new model, dubbed the slip-transpiration-vortex model, has been derived and tested for the flow in a channel with one wall patterned by blade riblets. The configuration with blades at the surface is probably the most difficult to simulate (in particular, with the growth of the pitch distance between blades) and previous attempts at modeling it have met with only partial success.

The procedure adopted here is based on asymptotic homogenization, with the advective term in the equations (formally of higher order) maintained at leading order because of indications from a preliminary scale analysis. Such advective terms are linearized around a streamwise-invariant base state which, in the *REV*, takes the form of a stationary vortex pair, with upwash along the side walls of the blades. The intensity of the vortices can be tuned by acting on the free parameter $\mathcal{P}$, but we have chosen here to employ the same range of intensities (and the same maximum upwash speed in the cross-section) for all ribs periodicities, to infer trends rather than to try and match available results.

The present model appears to be the most successful to-date in predicting the parabolic shape of the drag curve with ℓ^+, for the case of blade riblets; the key to its fortune lies in the fact that it retains advection, although in an approximate form, and it permits zero-net-mass-flux transpiration at the fictitious wall. On the negative side, it fails at capturing correctly the slip velocity or the near-wall Reynolds stress when ℓ^+ exceeds a value around 30. Such a threshold coincides with our expectations from the order of magnitude analysis of Sect. 2.1. Extending the model to higher order in the small parameter δ could possibly improve matters, and our current efforts are in this direction.

The applications of this study are not just limited to longitudinally-extended micro-grooves, because the procedure described can be applied to different kinds of textured walls, including those with relatively large amplitudes, provided Townsend similarity is not broken. The concept of equivalent sand-grain roughness is still commonly employed to identify geometric surface properties, even if it is by now accepted that such a concept fails to completely characterise roughness in many cases. It has been recently stated by Kadivar et al. [46] that "there is a need for a universal roughness scale that can describe every type of roughness and be used in any rough-flow regimes, including fully rough and transitionally rough regimes". We believe that the length (Navier slip) and surface area (interface permeability) coefficients identified here may represent these universal scales capable to discriminate different types of irregular surfaces; further work is clearly needed to support this conjecture.

As we look to the future, riblets hold promise for continued innovation in a range of fields. Among the topics for which research activities are expected to pay a dividend, we cite sinusoidal or converging–diverging (herringbone) micro-grooves. Also, bio-inspired designs can be pursued to further optimize riblet geometry and performance. Meanwhile, advancements in material science could lead to self-healing or adaptive riblet surfaces that adjust to different flow conditions in real-time, further enhancing their efficacy. With environmental concerns and fuel costs driving the need for efficiency across industries, riblet technology represents

a powerful tool for reducing energy losses and improving performance.

Author contributions AB designed the research plan, conducted microscopic simulations and wrote the main manuscript text. GI and ENA helped defining the scope of the study, conducted macroscopic simulations and prepared the figures. The authors analyzed together microscopic and macroscopic results and reviewed the final manuscript.

Funding Open access funding provided by Università degli Studi di Genova within the CRUI-CARE Agreement. This research was partially funded by the European Union - NextGenerationEU (*Piano Nazionale di Ripresa e Resilienza, Missione 4 Componente 2 Investimento 1.4 "Potenziamento strutture di ricerca e creazione di "campioni nazionali di R&S" su alcune Key Enabling Technologies"). Code CN00000023—Title: "Sustainable Mobility Center (Centro Nazionale per la Mobilità Sostenibile - CNMS)", CUP D33C22000940007.*

Data Availability No datasets were generated or analysed during the current study.

Declarations

Conflict of interest The authors declare no competing interests

References

1. Bechert DW, Bartenwerfer M (1989) The viscous flow on surfaces with longitudinal ribs. J Fluid Mech 206:105–129. https://doi.org/10.1017/S0022112089002247
2. Walsh MJ, Weinstein LM (1979) Drag and heat transfer characteristics of small longitudinally ribbed surfaces. AIAA J 17(7):770–771
3. Walsh MI (1980) Drag characteristics of V-Groove and transverse curvature riblets. In: In Viscous Flow Drag Reduction, G. R. Hough, Ed., AIAA Washington, DC, pp 168–184
4. Walsh MI, Lindemann AM (1984) Optimization and application of riblets for turbulent drag reduction. AIAA Paper 84–0374
5. Bechert DW, Bruse M, Hage W, Hoeven JGT, Hoppe G (1997) Experiments on drag-reducing surfaces and their optimization with an adjustable geometry. J Fluid Mech 338:59–87. https://doi.org/10.1017/S0022112096004673
6. Stars & Stripes Finds a Groove. The New York Times (1987). Section A, page 25. https://www.nytimes.com/1987/01/13/sports/scouting-stars-stripes-finds-a-groove.html
7. He Z, Mu L, Wang N, Su J, Wang Z, Luo M, Zhang C, Li G, Lan X (2023) Design, fabrication, and applications of bioinspired slippery surfaces. Adv Coll Interface Sci 318:102948. https://doi.org/10.1016/j.cis.2023.102948
8. Pakatchian MR, Rocha J, Li L (2023) Advances in riblets design. Appl Sci 13(19):10893. https://doi.org/10.3390/app131910893
9. Luchini P, Manzo F, Pozzi A (1991) Resistance of a grooved surface to parallel flow and cross-flow. J Fluid Mech 228:87–109. https://doi.org/10.1017/S0022112091002641
10. Luchini P (1996) Reducing the turbulent skin friction. In: Désidéri, J.A. (ed.) European Congress on Computational Methods in Applied Sciences and Engineering — Proceedings of 3rd ECCOMAS CFD Conference. Wiley, Chichester, England, U.K., pp 466–470
11. Jiménez J (2004) Turbulent flows over rough walls. Annu Rev Fluid Mech 36:173–196. https://doi.org/10.1146/annurev.fluid.36.050802.122103
12. Goldstein DB, Tuan T-C (1998) Secondary flow induced by riblets. J Fluid Mech 363:115–151. https://doi.org/10.1017/S0022112098008921
13. Endrikat S (2020) Effects of riblet shape on drag reduction in turbulent flow. University of Melbourne, Australia
14. Bottaro A (2019) Flow over natural or engineered surfaces: an adjoint homogenization perspective. J Fluid Mech 877:1. https://doi.org/10.1017/jfm.2019.607
15. Kamrin K, Bazant MZ, Stone HA (2010) Effective slip boundary conditions for arbitrary periodic surfaces: the surface mobility tensor. J Fluid Mech 658:409–437. https://doi.org/10.1017/S0022112010001801
16. Luchini P (2013) Linearized no-slip boundary conditions at a rough surface. J Fluid Mech 737:349–367. https://doi.org/10.1017/jfm.2013.574
17. Jiménez Bolaños S, Vernescu B (2017) Derivation of the Navier slip and slip length for viscous flows over a rough boundary. Phys Fluids 29:057103. https://doi.org/10.1063/1.4982899
18. Zampogna GA, Magnaudet J, Bottaro A (2019) Generalized slip condition over rough surfaces. J Fluid Mech 858:407–436. https://doi.org/10.1017/jfm.2018.780
19. Lācis U, Sudhakar Y, Pasche S, Bagheri S (2020) Transfer of mass and momentum at rough and porous surfaces. J Fluid Mech 884:21. https://doi.org/10.1017/jfm.2019.897
20. Bottaro A, Naqvi SB (2020) Effective boundary conditions at a rough wall: a high-order homogenization approach. Meccanica 55:1781–1800. https://doi.org/10.1007/s11012-020-01205-2
21. Ahmed EN, Bottaro A (2025) Exploring the nexus among roughness function, apparent slip velocity and

upscaling coefficients for turbulence over porous/textured walls. J Fluid Mech 1007:A24. https://doi.org/10.1017/jfm.2025.46
22. Wong J, Camobreco CJ, García-Mayoral R, Hutchins N, Chung D (2024) A viscous vortex model for predicting the drag reduction of riblet surfaces. J Fluid Mech 978:18. https://doi.org/10.1017/jfm.2023.1006
23. Orlandi P, Leonardi S (2006) DNS of turbulent channel flows with two- and three-dimensional roughness. J Turbul 7:73. https://doi.org/10.1080/14685240600827526
24. Orlandi P, Leonardi S, Antonia RA (2006) Turbulent channel flow with either transverse or longitudinal roughness elements on one wall. J Fluid Mech 561:279–305. https://doi.org/10.1017/S0022112006000723
25. Orlandi P, Leonardi S (2008) Direct numerical simulation of three-dimensional turbulent rough channels: parameterization and flow physics. J Fluid Mech 606:399–415. https://doi.org/10.1017/S0022112008001985
26. Modesti P, Endrikat S, Hutchins N, Chung D (2021) Dispersive stresses in turbulent flow over riblets. J Fluid Mech 917:55. https://doi.org/10.1017/jfm.2021.310
27. Robinson SK (1991) Coherent motions in the turbulent boundary layer. Annu Rev Fluid Mech 23:601–639. https://doi.org/10.1146/annurev.fl.23.010191.003125
28. Jiménez J (1994) On the structure and control of near wall turbulence. Phys Fluids 6(2):944–953. https://doi.org/10.1063/1.868327
29. Thakkar M, Busse A, Sandham ND (2018) Direct numerical simulation of turbulent channel flow over a surrogate for Nikuradse-type roughness. J Fluid Mech 837:1. https://doi.org/10.1017/jfm.2017.873
30. Bouthier M (1972) Stabilité linéaire des écoulements presque parallèles. J de Méc 11:1–23
31. Bouthier M (1973) Stabilité linéaire des écoulements presque parallèles. Partie II. La couche limite de Blasius. J de Méc 12:75–95
32. Gaster M (1974) On the effects of boundary layer growth on flow stability. J Fluid Mech 66:465–480. https://doi.org/10.1017/S0022112074000310
33. Saric WS, Nayfeh AH (1975) Nonparallel stability of boundary layer flows. Phys Fluids 18:945–950. https://doi.org/10.1063/1.861266
34. Itoh N (1986) The origin and subsequent development in space of Tollmien-Schlichting waves in a boundary layer. Fluid Dyn Res 1(2):119–130. https://doi.org/10.1016/0169-5983(86)90012-2
35. Smith FT (1979) On the non-parallel flow stability of the Blasius boundary layer. Proc R Soc A Math Phys Eng Sci 366(1724):91–109. https://doi.org/10.1098/rspa.1979.0041
36. Luchini P, Bottaro A (1998) Görtler vortices: a backward-in-time approach to the receptivity problem. J Fluid Mech 363:1–23. https://doi.org/10.1017/S0022112098008970
37. Sudhakar Y, Lācis U, Pasche S, Bagheri S (2021) Higher-order homogenized boundary conditions for flows over rough and porous surfaces. Transp Porous Media 136:1–42. https://doi.org/10.1007/s11242-020-01495-w
38. Mei CC, Vernescu B (2010) Homogenization Methods for Multiscale Mechanics. World Scientific Publishing Co, Singapore
39. Hecht F (2012) New development in freefem++. J Numer Math 20(3–4):251–265. https://doi.org/10.1515/jnum-2012-0013
40. García-Mayoral R, Jiménez J (2011) Drag reduction by riblets. Phil Trans R Soc A: Math Phys Eng Sci 369:1412–1427. https://doi.org/10.1098/rsta.2010.0359
41. García-Mayoral R, Jiménez J (2011) Hydrodynamic stability and breakdown of the viscous regime over riblets. J Fluid Mech 678:317–347. https://doi.org/10.1017/jfm.2011.114
42. Endrikat S, Modesti D, García-Mayoral R, Hutchins N, Chung D (2021) Influence of riblet shapes on the occurrence of Kelvin-Helmholtz rollers. J Fluid Mech 913:37. https://doi.org/10.1017/jfm.2021.2
43. Gómez-de-Segura G, Fairhall CT, MacDonald M, Chung D, García-Mayoral R (2018) Manipulation of near-wall turbulence by surface slip and permeability. J Phys Conf Ser 1001:012011. https://doi.org/10.1088/1742-6596/1001/1/012011
44. El-Samni OA, Chun HH, Yoon HS (2007) Drag reduction of turbulent flow over thin rectangular riblets. Int J Eng Sci 45:436–454. https://doi.org/10.1016/j.ijengsci.2007.03.002
45. Ahmed EN, Naqvi SB, Buda L, Bottaro A (2022) A homogenization approach for turbulent channel flows over porous substrates: formulation and implementation of effective boundary conditions. Fluids 7(5):178. https://doi.org/10.3390/fluids7050178
46. Kadivar M, Tormey D, McGranaghan G (2021) A review on turbulent flow over rough surfaces: fundamentals and theories. Int J Thermofluids 10:100077. https://doi.org/10.1016/j.ijft.2021.100077